Monthly Notices
of the
ROYAL ASTRONOMICAL SOCIETY

MNRAS **480,** 5517–5528 (2018)
Advance Access publication 2018 August 18

doi:10.1093/mnras/sty2264

Multiwavelength cross-correlations and flaring activity in bright blazars

I. Liodakis,[1]★ R. W. Romani,[1] A. V. Filippenko,[2,3]† S. Kiehlmann,[4] W. Max-Moerbeck,[5] A. C. S. Readhead[4] and W. Zheng[2]

[1]*KIPAC, Stanford University, 452 Lomita Mall, Stanford, CA 94305, USA*
[2]*Department of Astronomy, University of California, Berkeley, CA 94720-3411, USA*
[3]*Miller Institute for Basic Research in Science, University of California, Berkeley, CA 94720, USA*
[4]*Owens Valley Radio Observatory, California Institute of Technology, Pasadena, CA 91125, USA*
[5]*Departamento de Astronomía, Universidad de Chile, Camino El Observatorio 1515, Las Condes, Santiago, Chile*

Accepted 2018 August 15. Received 2018 August 15; in original form 2018 May 17

ABSTRACT

Blazars are known for their energetic multiwavelength flares from radio wavelengths to high-energy γ-rays. In this work, we study radio, optical, and γ-ray light curves of 145 bright blazars spanning up to 8 yr, to probe the flaring activity and interband correlations. Of these, 105 show $>1\sigma$ correlations between one or more wavebands, 26 of which have a $>3\sigma$ correlation in at least one wavelength pair, as measured by the discrete correlation function. The most common and strongest correlations are found between the optical and γ-ray bands, with fluctuations simultaneous within our $\sim$30 d resolution. The radio response is usually substantially delayed with respect to the other wavelengths with median time lags of $\sim$100–160 d. A systematic flare identification via Bayesian block analysis provides us with a first uniform sample of flares in the three bands, allowing us to characterize the relative rates of multiband and 'orphan' flares. Multiband flares tend to have higher amplitudes than 'orphan' flares.

Key words: relativistic processes – galaxies: active – galaxies: jets.

1 INTRODUCTION

Blazars are luminous and highly variable across the entire electromagnetic spectrum. Their emission, dominated by relativistically boosted jets, shows a spectral energy distribution with two distinct humps. The low-energy peak (radio to ultraviolet, and in some cases X-rays) is thought to be produced by synchrotron radiation, and the high-energy hump (X-rays to high-energy γ-rays) is likely Compton emission. However, the source of the seed photons that produce the observed high-energy emission is not fully understood. Some models also attribute γ-ray flux to proton-mediated emission rather than inverse-Compton scattering. Traditionally, blazars are classified by their optical spectral line properties as BL Lacertae objects (BL Lacs; broad lines typically lost against a bright continuum) and flat-spectrum radio quasars (FSRQs; strong, broad lines).

Blazars exhibit violent flaring, in which the Earth-directed flux can increase by orders of magnitude over short time-scales. Flares appear in multiple wavebands either simultaneously or with a time delay ranging from days to months. These delays can provide clues to the emission process and the relative location of the emitting region at different wavelengths. Flaring events are often accompanied by other phenomena such as the ejection of jet components mapped at very long baseline interferometry (VLBI) scales (e.g. Marscher et al. 2008) and rotations of the optical polarization plane (e.g. Blinov et al. 2017). The origin of the γ-rays in particular is poorly understood. The most likely mechanism appears to be inverse-Compton (IC) scattering of lower-energy photons by the relativistic jet electrons. However, the nature of the incident photon field and the location of the upscattering electrons are poorly constrained. If the incident photon field is external to the jet (accretion disc, broad-line region, etc.), the IC scattering is referred to as external Compton (EC, e.g. Dermer, Schlickeiser & Mastichiadis 1992), while if the incident photons are from the jet itself it is called synchrotron self-Compton (SSC, e.g. Abdo et al. 2010b). One can probe these uncertainties by studying the correlated variability between different frequency bands.

Several monitoring programs have followed γ-ray-loud blazars at various wavelengths since the launch of the *Fermi gamma-ray space telescope*, with the primary goal of constraining the mechanism and location of the γ-ray emission through time-series analysis. This is usually accomplished through the cross-correlation of radio and γ-ray light curves (e.g. Fuhrmann et al. 2014; Max-Moerbeck et al. 2014; Ramakrishnan et al. 2015), or optical and γ-ray light curves (e.g. Patiño-Álvarez et al. 2013; Cohen et al. 2014; Hovatta et al. 2014; Ramakrishnan et al. 2016). An alternative approach is to organize intensive multiwavelength campaigns of individual sources (e.g. Rani et al. 2013; Karamanavis et al. 2016).

★ E-mail: ilioda@stanford.edu
† Miller Senior Fellow

In this work, we revisit the optical–γ-ray (Cohen et al. 2014) and γ-ray–radio correlations (Max-Moerbeck et al. 2014) as well as the underexplored optical–radio correlation using long-term monitoring of a large sample of γ-ray-bright blazars. Our goal is to apply statistical analysis to reveal correlation trends and compare them across blazar classes. We present the sample and the results of basic cross-correlation analysis in Section 2. In Section 3 we use the correlations to associate individual flares seen in different wavelengths and examine the statistical properties of the correlated and non-correlated 'orphan' events. Section 4 discusses our findings and summarizes our conclusions.

2 SAMPLE AND CROSS-CORRELATION RESULTS

We use data from the Owens Valley Radio Observatory (OVRO; 15 GHz) 40-m telescope[1] (Richards et al. 2011), the 0.76-m optical Katzman Automatic Imaging Telescope (KAIT; unfiltered charge-coupled device exposures roughly corresponding to the *R* band) at Lick Observatory[2] (Filippenko et al. 2001; Li et al. 2003), and the monthly averaged Large Area Telescope (LAT) γ-ray light curves from *Fermi*[3] (Acero et al. 2015). The γ-ray light curves are automatically generated through aperture photometry using PASS8 and the latest FTOOLS package.[4] The photometry is in the 0.1–200 GeV range with a 1 deg radius aperture on a monthly cadence, though observations <5 deg from the Sun have been excluded. OVRO and KAIT have been monitoring blazars since 2007 and 2009, respectively, in support of *Fermi*. Both programs run in a fully automated mode with an approximate cadence of 3 d. The full description of the reduction pipelines for both KAIT and OVRO can be found in Li et al. (2003) and Richards et al. (2011), respectively. The sources in our sample common to these programs are all relatively bright objects from the first LAT blazar catalogue (Abdo et al. 2010a). The optical and γ-ray light curves are publicly available online, while the radio light curves are publicly available through the OVRO team. In this work we are considering observations from 2008 January until 2017 May for the radio, 2009 July until 2017 November for the optical, and 2008 August until 2017 November for the γ-rays.

Our final sample consists of the 145 common sources between OVRO, KAIT, and *Fermi*, 93 of which are BL Lacs, 47 are FSRQs, and 5 are as yet unclassified sources. Sample light curves showing strong intraband correlations are shown in Fig. 1. To probe these correlations quantitatively, we calculate the discrete correlation function (DCF; Edelson & Krolik 1988) for each pair of wavebands. For two time series with observations $[x_1, x_2, ...x_n]$, $[y_1, y_2, ...y_n]$, the DCF is defined through the unbinned discrete correlation

$$\mathrm{UDCF}_{ij} = \frac{(x_i - \langle x \rangle)(y_j - \langle y \rangle)}{\sqrt{(\sigma_x^2 - e_x^2)(\sigma_y^2 - e_y^2)}}, \quad (1)$$

where (x_i, y_j) are the observations, $(\langle x \rangle, \langle y \rangle)$ are the mean of each light curve, (σ_x, σ_y) are the standard deviation, and (e_x, e_y) are the average uncertainty, as

$$\mathrm{DCF}_\tau = \frac{1}{N}\mathrm{UDCF}_{ij}, \quad (2)$$

where N is the number of (x_i, y_j) pairs for which $\tau - \Delta\tau/2 \leq t_j - t_i \leq \tau + \Delta\tau$. The standard error of the DCF is defined as (Edelson & Krolik 1988)

$$\sigma_{\mathrm{DCF}(\tau)} = \frac{1}{N-1}\left[\sum \left(\mathrm{UDCF}_{ij} - \mathrm{DCF}_\tau\right)^2\right]^{1/2}. \quad (3)$$

We explored time lags between −1000 and 1000 d, a range chosen so that for any given time lag at least 2/3 of the light curves would be overlapping. This ensures a robust estimation of the DCF time lags, especially for the optical light curves where the observing gaps additionally reduce the periods of overlap with other wavelengths. The time-lag bins were set to the average cadence of the less frequently sampled light curve to ensure at least a few tens of pairs in each bin for a better determination of the uncertainty of the DCF. The entire data set of each wavelength was used in the calculation of the DCF. Once a DCF peak was identified, we fitted it with a Gaussian function to best determine the cross-correlation coefficient at the peak as well as the peak-weighted time lag (τ) and its uncertainty (σ_τ).

For each blazar and each waveband, we generated a distribution of random cross-correlation functions, using the comparison waveband curves of all other sources (Cohen et al. 2014). This generates a distribution of statistical fluctuations in the DCF for each time-lag bin, using light curves with sampling and variability properties similar to those of the target source. In the optical band we restrict the random cross-pairs to objects with right ascension (RA) within 3 h. This ensures that the seasonal coverage, and hence the observation window function, are similar. This process results in ∼5000 false-pairs for optical–γ-ray and optical–radio cross-correlations and ∼20 000 false-pairs for the γ-ray–radio comparison. From this distribution of false-pair matches we estimate the median and 1σ, 2σ, and 3σ confidence intervals for each time-lag bin. Using the false-pair distribution to measure the statistical fluctuations we quote the peak significance for each source, given as σ confidence level (note that the 'σ' are thresholds for the standard probability intervals; the false significant distributions are not strictly Gaussian).

From the confidence intervals we estimate the significance of the peak in the real cross-correlation coefficient of interest. Fig. 2 shows one example with the optical–γ-ray and optical–radio DCFs for J2236-1433. In this case the optical–γ-ray correlation exceeds 3σ, while the γ-ray–radio peak significance is only $\sim 1\sigma$. The peak measurements and significances for all pairs with a $>1\sigma$ correlation are given in the Appendix (Table A1).

2.1 Optical–radio cross-correlation

The optical–radio cross-correlation analysis yielded 58 sources with a $>1\sigma$ correlation coefficient. BL Lacs account for 31 sources, 26 are FSRQs, and 1 is unclassified. Fig. 3 shows the distribution of time lags with $>1\sigma$ correlation coefficients for the BL Lacs and FSRQs. Here positive time lags indicate optical peaks leading the radio. Clearly the majority of sources (89.6 per cent) show positive time lags. Using the two-sample Kolmogorov-Smirnov (K-S) test,[5] we do not find any significant difference between the BL Lac and FSRQ time lags (43.8 per cent probability that the two samples are drawn from the same distribution). There are three BL Lacs and

[1] http://www.astro.caltech.edu/ovroblazars/
[2] http://herculesii.astro.berkeley.edu/kait/agn/
[3] https://fermi.gsfc.nasa.gov/ssc/data/access/
[4] More details on the different steps for the aperture photometry are available online, https://fermi.gsfc.nasa.gov/ssc/data/analysis/scitools/aperture_photometry.html

[5] The two-sample K-S test operates under the null hypothesis that the two samples are drawn from the same distribution. For any probability value >5 per cent we cannot reject the null hypothesis.

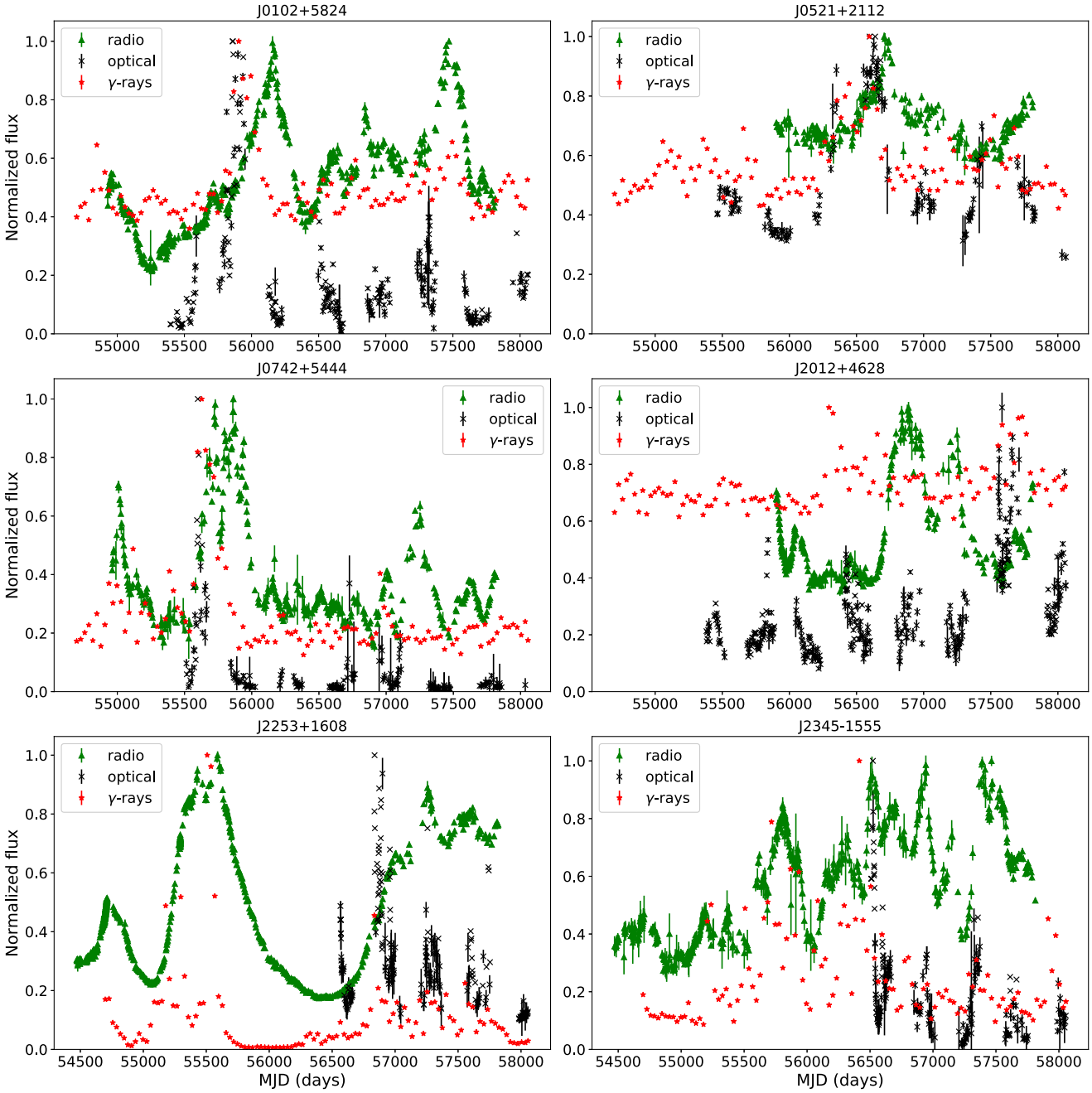

Figure 1. Radio, optical, and γ-ray light curves of six sources with $>1.5\sigma$ correlation coefficient in all three pair combinations, normalized to the highest flux of each light curve. Green '▲' are for radio, black 'x' for optical, and red '⋆' for γ-ray observations.

one FSRQ with a $>3\sigma$ significant time lag. Out of the sources with $>3\sigma$ significant time lags all but one BL Lac (J1959+6508) have positive time lags. From the distribution of significances, out of the 58 sources that showed at least a $>1\sigma$ correlation we estimate that 5.8 will be false positives; in the $>2\sigma$ set we should have no more than 0.6 false correlations.

2.2 Optical–γ-ray cross-correlation

For the optical–γ-ray DCFs we found 73 sources (42 BL Lacs and 31 FSRQs) with a $>1\sigma$ correlation peak (Fig. 4). Positive time lag indicates an optical peak leading the γ-rays. Again, there is no significant difference between the BL Lac and FSRQ time lags (a K-S test yielded a 30.3 per cent probability). The distribution of time lags is narrow with the majority of sources showing time lags between [−50,50] d, while roughly half the sources have time lags consistent with zero (within 3σ), suggesting nearly coincident optical and GeV radiation zones. However, the 30 d cadence of the LAT light curve clearly limits our ability to probe short time-scales. In order to assess whether the 30 d sampling of the light curves is affecting the derived time lags and thus our overall results, we repeated the above analysis for eight sources with publicly available 7 d light curves included in the LAT monitored list. Fig. 5 shows the comparison of the derived time lags for the two different binnings

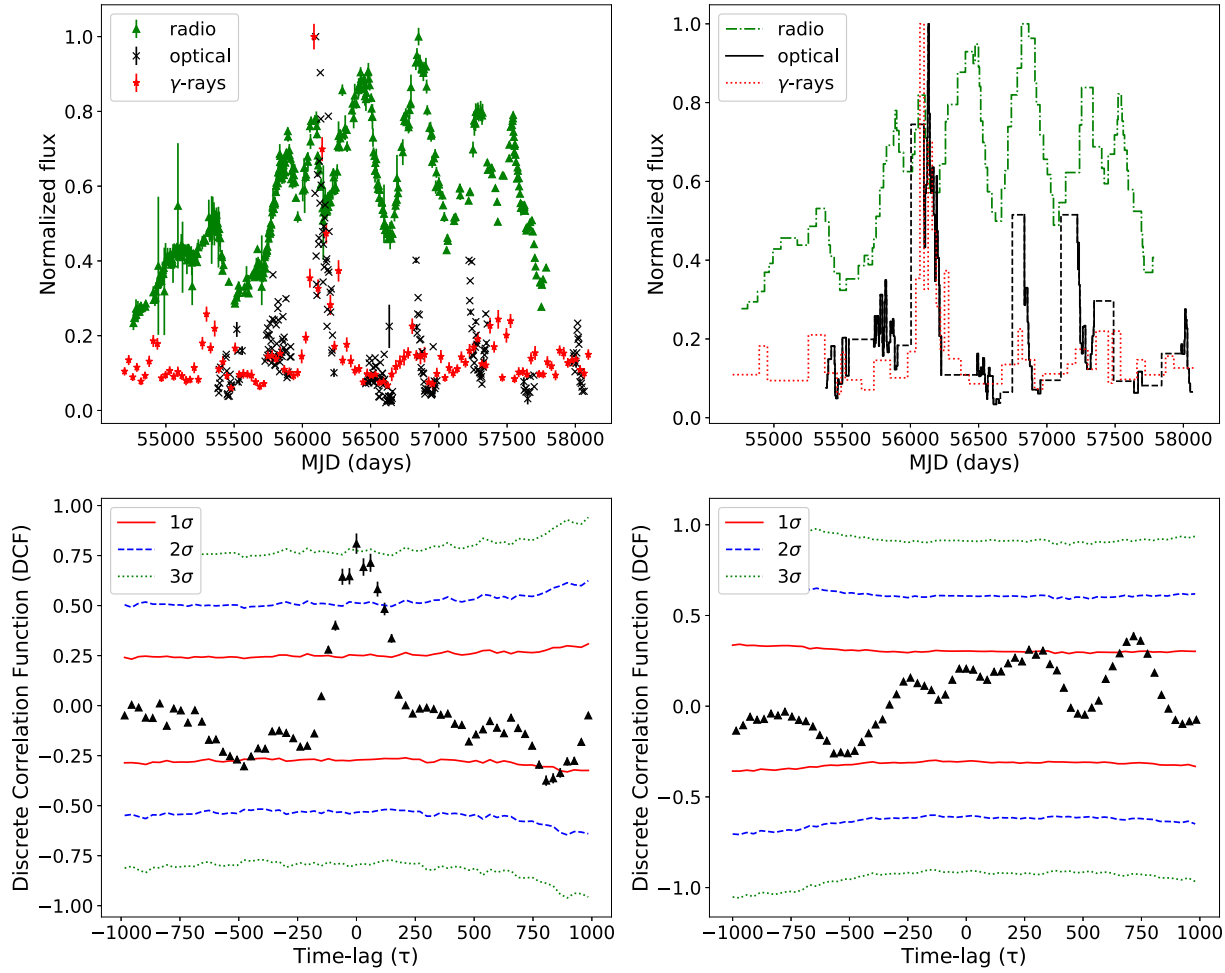

Figure 2. Upper panel: Radio, optical, and γ-ray light curves for J2236-1433 normalized to the highest flux of each light curve (left-hand side, symbols, and colours as in Fig. 1) and the Bayesian block representation of the same light curves (right-hand side, dash-dotted green for radio, solid black for optical, dotted red for γ-rays). The dashed segments in the optical light curve denote the observing gaps. Lower panel: Discrete correlation function for the optical–γ-ray light curves (left-hand side) and the γ-ray–radio light curves (right-hand side). The red solid, blue dashed, and green dotted lines mark the 1σ (68 per cent), 2σ (95 per cent), and 3σ (99.7 per cent) confidence intervals.

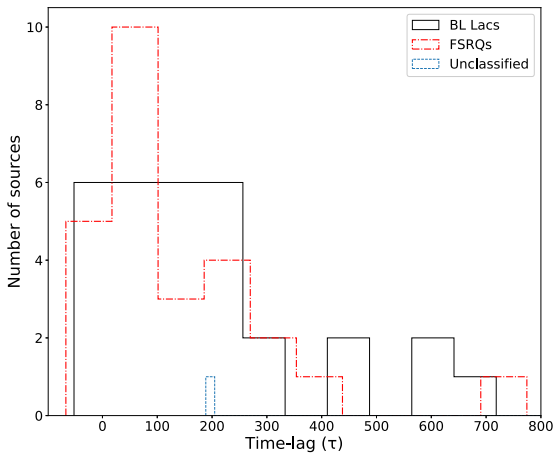

Figure 3. Distribution of the time lags between the optical and radio emission for BL Lacs (solid black), FSRQs (dash-dotted red), and unclassified sources (dashed blue). Positive time lags indicate that the optical emission is leading the radio.

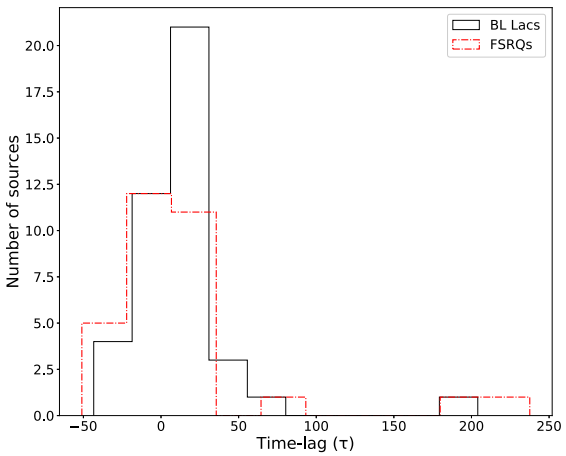

Figure 4. Distribution of the time lags between the optical and γ-ray emission for BL Lacs (solid black) and FSRQs (dash-dotted red). Positive time lags indicate that the optical emission is leading the γ-ray.

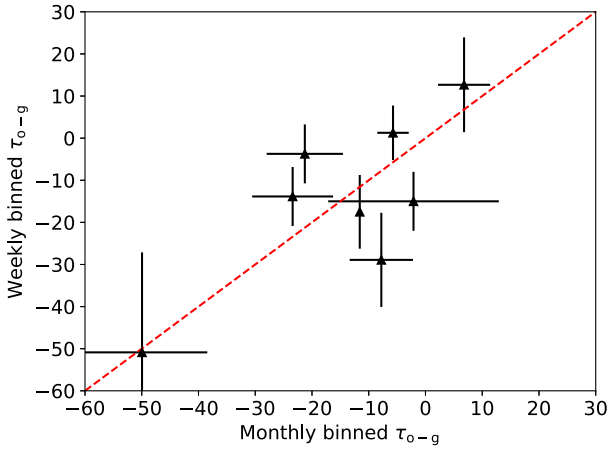

Figure 5. Comparison between the optical–γ-ray time lags derived for 30 and 7 d binned light curves. The red dashed line marks the one-to-one relation.

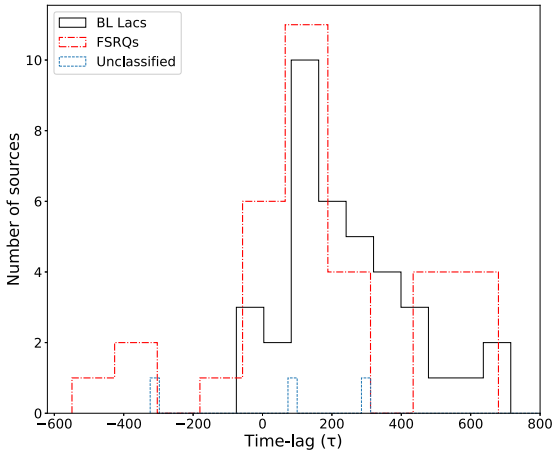

Figure 6. Distribution of the time lags between the radio and γ-ray emission for BL Lacs (solid black), FSRQs (dash-dotted red), and unclassified sources (dashed blue). Positive time lags indicate that γ-rays are leading the radio emission.

of the *Fermi* data. The derived time lags are consistent within the uncertainties.

To investigate whether there is a systematic bias introduced by the coarser bins, we fit a line to the time lags derived by the two differently binned light curves taking the uncertainties into account. For the optical–γ-ray time lags we find a slope of 0.9 ± 0.3. For the γ-ray–radio time lags we find a slope 1.1 ± 0.1, although it should be noted that in this case there are only four sources that show a correlation (see Section 2.3). In both cases the intercept is consistent with zero. These tests would suggest that although it will undoubtedly be productive to repeat this analysis with a more finely sampled LAT light curve at least for the sources with bright flares, the coarser binning is not biasing our results for the time lags in any significant way.

The false positives in the optical–γ-ray case are estimated to be no more than 4.7 sources, 0.9 above 2σ. There is one BL Lac object (J0045+2127) with the optical leading the γ-rays by roughly 200 d (2σ). Considering the typical radio lag noted above, we might speculate that for this source the γ-rays are produced closer to the radio core. However, J0045+2127 is radio-faint and does not provide a significant γ-ray–radio DCF peak (see Table A1), preventing us from seeing the small lag that would be then expected.

2.3 γ-ray–radio cross-correlation

Finally, the γ-ray–radio cross-correlation analysis yielded 73 sources with a cross-correlation coefficient greater than 1σ, 37 of which are BL Lacs, 33 FSRQs, and 3 unclassified sources (Fig. 6). Positive time lags means that the γ-rays are leading the radio emission. We estimate 8.2 of 73 $> 1\sigma$ cross-correlations and 0.5 of the $>2\sigma$ cross-correlations are false. Again, the K-S test showed no significant difference between the BL Lac and FSRQ time lags (15.3 per cent probability). The majority of sources (84.9 per cent) and all the $>3\sigma$ significance sources (2 BL Lacs) have positive time lags; the radio peaks are strongly delayed from the γ-ray (and optical) flares.

By comparing the unlagged light curves of Fig. 1 with the correlation peak lags in Table A1 of the Appendix , one can visualize the expected shifts. Each of these sources has at least $>1.5\sigma$ for all three DCF peaks.

2.4 Comparison with other studies

Earlier investigations typically measure only a single wavelength pair, but it is worth comparing our results with these studies' findings.

Max-Moerbeck et al. (2014) investigated the γ-ray–radio correlation using data from OVRO and *Fermi*, but with a shorter time span (about 3–4 yr). They estimated the significance of the DCF correlation coefficient by creating simulated light curves with statistical properties similar to those of the actual targets, using Monte-Carlo simulations and assuming a power-law power spectral density model. The few common sources with this work show low-significance DCF peaks ($<2\sigma$, 22 sources). There are a few additional sources for which the reported time lag is not detected in this study. Given the low significance of these correlations as well as the longer light curves considered here, we conclude that the previously reported correlations were false positive. Out of 41 sources, they found three sources with a highly significant correlation ($>2.25\sigma$) in all of which the γ-ray emission led the radio. Although these three sources are not included in our study, our work provides additional evidence for the γ-ray–radio lag noted there (Fig. 6).

Zhang et al. (2017) investigated the optical–radio correlation using data from KAIT and OVRO. They considered 70 common sources and found 55 sources with a significant correlation (DCF correlation coefficient >0.5). For the determination of the time lag and its uncertainty they used the flux redistribution method (Peterson et al. 1998). They also find a strong trend for the optical to lead the radio. Of the common sources with a significant correlation, only one source (J1748+7005) appears to be inconsistent. However, it shows a low-significance DCF peak in both studies ($\sigma_{\rm DCF} = 1.23$, this work; DCF $= 0.64$, Zhang et al. 2017), suggesting a higher probability for a false-positive correlation. There are a handful of sources that have a $>1\sigma$ correlation (all of which are $<2\sigma$) in our study yet do not appear to have a significant correlation in Zhang et al. (2017; DCF <0.5), and vice versa. These discrepancies are most likely attributed to the differences in the adopted methodologies. It is reassuring that most of these cases are in the low-significance range for both studies.

Cohen et al. (2014) investigated the optical–γ-ray correlation using data from KAIT and *Fermi*; our DCF methods follow this

work. There are important differences: they only studied the 39 brightest sources in optical and γ-rays, with a common time span of <5 yr. However, their use of adaptive binning (Lott et al. 2012) allowed a better probe of small time lags τ, albeit for only a few sources with very bright flares.[6] Cohen et al. (2014) find correlations for 23/39 sources at $>1\sigma$. Still, the finer LAT sampling from the adaptive binning may have revealed a few additional short flares, so such reanalysis could be productive. Of the sources in common, we generally have a substantially higher peak DCF significance. For the common well-detected sources, the measured lags for 19 are consistent, while the remaining sources are either listed as < 68 per cent significance or show small τ which are not well resolved in this work given the sampling of our LAT light curves. We do find four additional correlations not reported by Cohen et al. (2014). With a larger set of sources (and more flares) to compare, our study is more sensitive to differences between the source classes (e.g. BL Lac/FSRQ differences, although no strong trends are seen even with our larger sample).

A three-band correlation analysis was performed by Ramakrishnan et al. (2016) for 15 sources using observations spanning 2.5 yr. They used optical, γ-rays, and two radio frequencies (37 and 95 GHz). Their methodology for estimating the DCF and its significance is similar to that of Max-Moerbeck et al. (2014). For the two sources that show an optical–radio correlation in Ramakrishnan et al. (2016) at 37 GHz, we find larger time lags. This is expected given that 15 GHz typically probes regions farther downstream in the jet than 37 GHz. For the common sources with an optical–γ-ray correlation we find time lags consistent within the uncertainties. We have derived time lags for two sources (J0808-0751, J2232+1143) listed without a correlation in Ramakrishnan et al. (2016), most likely owing to the longer time span of the observations considered in this work. Generally, although our radio observations are at 15 GHz, and their *Fermi* light curves are produced using weekly bins, we reach similar conclusions.

3 CORRELATED FLARING ACTIVITY

3.1 Flare identification

We also want to examine the properties and correlations of individual flaring events. To this end we subjected the light curves to Bayesian block analysis (Scargle et al. 2013), which is a method of segmenting the light curves in 'blocks' so that all the observations within each block are statistically consistent with a constant value. The only parameter of the method is the prior of the slope for the number of blocks, which was set to ncp_prior ≈ 3 for all three bands. Bayesian blocks allow us to model the flux variations in the light curves and obtain a relatively uniform and unbiased list of flare times and flare amplitudes in each band. Flares were identified as local (centre of three blocks) maxima. Since every significant local maximum is counted as a flare, this gives a large rate in highly variable bands, such as the optical.

An example of Bayesian block decomposition is shown in Fig. 2. This analysis yielded 1284 radio flares, 2465 optical flares, and 732 γ-rays flares in the full survey. The large optical band flare rate may, in part, be caused by the relatively small photometric errors adopted from KAIT aperture photometry. A few 'flares' may also be due to poor acquisition (bright stars in the aperture) or other

[6]We should note that their sign convention for τ_{og} is opposite to that used here.

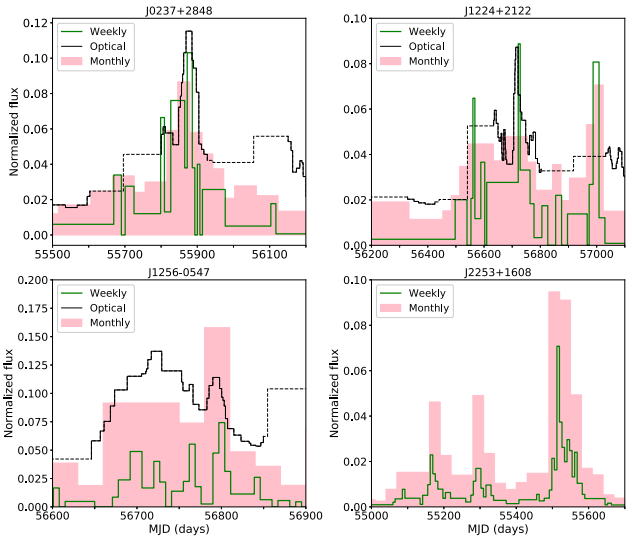

Figure 7. Bayesian block representation of the normalized optical, 7 d, and 30 d light curves for four sources: J0237+2848 (upper left-hand side), J1224+2122 (upper right-hand side), J1256-0547 (lower left-hand side), and J2202+4216 (lower right-hand side). The light curves have been aligned according to the cross-correlation results. Solid black is for the optical, dotted green for the 7 d binned, and the red shaded area for the 30 d binned light curves. The dashed segments in the optical light curve denote the observing gaps.

systematic photometric errors. We have, however, visually inspected the light curves to remove the most obvious of such events. It is thus interesting that there are a factor of ∼3.5 more optical flares than γ-ray events. This is even more significant since ∼40 per cent of the optical light curve is lost to seasonal and other gaps, and an additional ∼10 per cent is close enough to gap edges to hinder flare detection. In part we expect that this is due to the coarse γ-ray sampling (∼30 versus ∼3 d).

Fig. 7 shows the Bayesian block representation for four sources with available weekly binning γ-ray data. The 7 d binned light curves appear to trace the optical variability better, which could potentially improve the flare association by reducing the number of falsely matched peaks and decreasing the number of unassociated flares in the optical (see discussion below). However, overall the 30 d binned light curves adequately trace the flaring events in both the 7 d binned and optical light curves. Considering all the available 7 d light curves, we find 18–66per cent (average ∼50 per cent) more flares than in the 30 d light curves. Including this correction, the expected number of γ-ray flares for the entire sample is comparable to the radio, yet interestingly still less than the optical (Table 1). One can speculate that a number of low-amplitude flares have occurred in periods where only γ-ray upper limits are available from the 7 d bins; limited γ-ray counts prevent their detection.

The radio flaring rate is intermediate. Here the decrease from the optical may be attributed to the radio emission typically varying on longer time-scales. Many flare complexes are seen as overlapping peaks, and so inevitably some peaks are lost in the block analysis because of this smoothing.

3.1.1 Multiwavelength flaring rates

Generally, FSRQs tend to exhibit more flares per source than the BL Lacs in radio and γ-rays, while BL Lacs show more flares in optical. This may be attributed to FSRQs being optically dominated

Table 1. Total and associated radio, optical, and γ-ray flares.[a]

	Radio	Optical	γ-ray
Radio	1284	183/433(235)	217/686
Optical	159/903	2465	165/1361
γ-ray	159/376	174/384(203)	732
Median Fl. rate	1.10	2.54	0.84

Note: [a]Diagonal entries give the total number of flares in each waveband. Off-diagonal entries: the numerator gives the number of associated flares in the row band with flares in the column band; the denominator indicates the total number of flares in the row band; parentheses show the number of flares within periods of time with optical coverage (i.e. not within an optical observing gap). For example, in the entry in the first row, second column [183/433(235)], the numerator gives 183 associated radio flares with an optical counterpart in sources with an optical–radio correlation, the denominator indicates 433 radio flares in these sources, and the parentheses (235) give the number of flares during the optical observing season. The last row reports the median flaring rate for each wavelength in flares yr^{-1} per source.

by thermal emission from the accretion disc (e.g. Bonning et al. 2012). For sources with an optical–radio correlation, FSRQs have an average of 2.3 flares yr^{-1} source^{-1} in optical and 1.3 flares yr^{-1} source^{-1} in radio. BL Lacs showed 3.6 flares yr^{-1} source^{-1} in optical and 1.0 flares yr^{-1} source^{-1} in radio. FSRQs with an optical–γ-ray correlation displayed similar flare rates in optical (2.5 flares yr^{-1} source^{-1}) and 0.8 flares yr^{-1} source^{-1} in γ-rays. BL Lacs exhibit a slightly higher number of flares in optical (3.7 flares yr^{-1} source^{-1}) and 0.5 flares yr^{-1} source^{-1} in γ-rays. For the sources with a γ-ray–radio correlation, FSRQs show 1.1 flares yr^{-1} source^{-1} and 0.7 flares yr^{-1} source^{-1} and BL Lacs have 0.9 flares yr^{-1} source^{-1} and 0.3 flares yr^{-1} source^{-1} in radio and γ-rays, respectively. Ramakrishnan et al. (2015) made a similar Bayesian block analysis with a smaller sample, finding that sources with a γ-ray–radio correlation have 1.2 flares yr^{-1} source^{-1} in γ-rays and 0.6 flares yr^{-1} source^{-1} in radio.

The higher flare rates seen in γ-rays for the sample considered by Ramakrishnan et al. (2015) may be attributed to their weekly binned *Fermi* light curves. Indeed, repeating the analysis on the 7 d light curves, we find that the sources show ∼1.3 flares yr^{-1} on average. Similarly, their lower flaring rate at radio wavelengths could be caused by OVRO having twice the cadence of the Metsähovi monitoring program. If the radio flares are connected to the ejection of new jet components (e.g. Savolainen et al. 2002), we would expect to find a similar ejection rate from VLBI studies. Results from the MOJAVE survey for the 1.5 Jy flux-limited sample imply a lower ejection rate (∼0.83 ejections yr^{-1} on average; Lister et al. 2009) than suggested by the flaring rate found in this work. Either the faster cadence of the OVRO survey allows us to identify flares that are missed or are not well resolved in the VLBI maps, or a small fraction of these flares are random fluctuations not connected to the ejection of a new jet component. On the other hand, at 43 GHz the ejection rate is higher (∼1.25 ejections yr^{-1} on average; Jorstad et al. 2017). Given the longer radio time response at 15 GHz, this suggests that some individual events identified in this work might in fact be the superposition of multiple flares that could in principle be resolved at a higher frequency.

Sources that have a significant correlation between at least one pair of wavelengths show on average 1.1 flares yr^{-1} source^{-1} in radio, 2.4 flares yr^{-1} source^{-1} in optical, and 0.5 flares yr^{-1} source^{-1} in γ-rays. Sources that did not exhibit any significant multiwavelength correlation have a lower flare rate on average (0.6 flares yr^{-1} source^{-1} in radio, 2.2 flares yr^{-1} source^{-1} in optical, and 0.2 flares yr^{-1} source^{-1} in γ-rays). Of course, this may be a selection effect, as in sources that show fewer flaring events the light-curve fluctuations are more likely to be dominated by uncorrelated stochastic variations weakening the DCF peaks. Overall, there are 5.4 per cent less optical flares, 42 per cent less radio, and 59 per cent less γ-ray events in sources without any significant correlation compared to sources with a significant correlation between at least one pair of wavelengths.

3.1.2 *Associated and orphan flares*

After identifying the flares, we focus on the sources showing at least one significant interband correlation. This allows us to align the light curves using the measured DCF τ and make interband identifications. We consider a flare to be coincident if the Bayesian block of the peak bins overlaps in the two wavebands. We are also interested in 'orphan' flares, seen in one band but not another. These have been noted in past studies (e.g. Krawczynski et al. 2004; Rani et al. 2013), but it has not previously been possible to make statistical statements about the fraction of unassociated events. Table 1 gives the number of coincident flares in each waveband over the number of flares in correlated sources for the comparison waveband. For the optical we must exclude the time in the seasonal gaps, so we list in parenthesis the number of flares not in gaps.

The first statistic to note is that the high optical flare rate leads to a high coincidence rate – fully 78 per cent of the radio flares in correlated optical sources during the observing window have correlated optical flares. Similarly 86 per cent of γ-ray flares during correlated active optical observations have an optical counterpart. With the wide radio blocks and the 30 d γ-ray sampling, some of these associations are doubtless false coincidences. To quantify this false-pair pollution, we repeat the same analysis for sources with at least a 2σ significant correlation but randomly misalign the light curves with shifts of up to 300 d and compute the number of 'associated' flares. This suggests that roughly 18 per cent of radio and 28 per cent of γ-ray flares could be falsely associated with an optical counterpart. The higher percentage of false γ-ray associations is most likely caused by the lower cadence and coarser blocking of the γ-ray light curves. For sources with a γ-ray–radio correlation, fewer than 10 per cent of either radio or γ-ray flares could be falsely associated. Still, we infer that we have identified true associations for ∼60 per cent of the radio and γ-ray flares. Unsurprisingly, with the high optical flare rate most are unassociated, with only 18 per cent showing radio counterparts and 12 per cent γ-ray counterparts. In contrast, comparing the radio and γ-rays directly, we see that 32 per cent of the radio flares show associated γ-ray events, while 42 per cent of the γ-ray flares appear also in the radio. We conclude that (at least to our non-uniform sensitivity) over half of the radio/γ-ray events are mutual orphans. While most events have optical associations, and while the fact that we get highly significant correlations means that a fair fraction of these must be real, the high density of optical events does introduce some false pairs.

BL Lacs and FSRQs show a similar percentage of associated radio (∼77 per cent) and γ-ray (83–88 per cent) flares with an optical counterpart. FSRQs have roughly 20 per cent of their optical flares associated with either a radio or a γ-ray flare. The percentages are significantly lower for BL Lacs (15.9 per cent associations with radio and 8.4 per cent associations with γ-ray flares). For sources with a γ-ray–radio correlation, 36–41 per cent of flares in FSRQs

are associated between the two wavelengths. BL Lacs have fewer associated radio (24.7 per cent) than γ-ray flares (42.8 per cent).

Repeating the flare-association analysis on the 7 d light curves, we find an increase in the orphan γ-ray events for the sources with a γ-ray–radio correlation (although in this case only four sources are considered). For the sources with an optical–γ-ray correlation there is an improvement in the flare association. We find that roughly 24 per cent of the optical and 91 per cent of the γ-ray flares (an improvement of $\sim$+6 per cent) are now associated with a counterpart. It is interesting that even with a factor of 4 improvement in the sampling of the γ-ray light curves, there is only a small reduction in the number of orphan optical events. This suggests that although repeating the analysis with more finely binned light curves for the entire sample would undoubtedly be beneficial, our statistical results and conclusions are not strongly affected by the choice of coarser bins.

3.2 Flare amplitude distributions

Our Bayesian block analysis also lets us compare the flare amplitude distributions. We compute the flare flux density by computing the weighted average flux density within the lowest 20 per cent of the entire light curve as a background/quiescence level and subtracting this from the flux density in the peak block. We can then compare the amplitude distributions of various sources (and source groups) using the Wilcoxon rank-sum (WRS) test.[7]

One useful comparison is between the associated and orphan flares. For example, taking optical–radio and optical–γ-ray correlated sources, the associated flares are distinctly brighter than the orphan sets (WRS p-value $< 10^{-4}$ per cent for all these bands). In contrast, for the γ-ray–radio correlated sources the orphan γ-ray flares are consistent with the correlated set (30.9 per cent) while the associated radio flares are brighter at a statistically significant ($P \approx 10^{-13}$ per cent) level. This would hint that the mechanisms driving the two wavebands' events are not strictly proportional.

4 DISCUSSION AND CONCLUSIONS

In this work we have investigated the temporal correlations between the optical, radio, and γ-ray emission of a large sample of blazars. Out of the 145 sources, 105 revealed at least one $>1\sigma$ significant correlation coefficient between wavebands. Out of these, 38 showed a correlation in only one pair of wavelengths, 35 in two pairs, and 32 in all three pairs. Based on the significance of DCF peaks, we estimated that only 9.8 per cent of the optical–radio, 6.4 per cent of the optical–γ-ray, and 11.2 per cent of the γ-ray–radio cross-correlations will be false positives. For the sources with a $>2\sigma$ significant correlation the false-positive rate is roughly 2 per cent in any wavelength pair. It should be noted that blazars exhibit a wide variety of flaring patterns and behaviours which could be the result of different mechanisms operating even in the same source (e.g. Chen et al. 2012; Liodakis et al. 2017). It is possible for a source to show both correlated and uncorrelated events with other wavelengths, which can impact the significance of DCF. This could explain why many of our sources show only a 1σ or 2σ significant DCF peaks. Our results are qualitatively consistent with those of previous studies, but our longer time base has allowed us to identify a larger number of, and more significant, correlations. Continued monitoring would doubtless improve the situation further.

We find that the optical–γ-ray time lags are generally small, while both lead the radio by $\sim$30–150 d. However, there are three sources (J0433+2905, J1849+6705, and J2236+2828) in which all three wavelengths are correlated with lags $<$30 d. In fact, unusually, J0433+2905 shows the optical emission coming 20–30 d earlier than both radio and γ-rays (the other two are more conventional). This suggests that the emission regions are located in close proximity. The fact that there is a strong connection between optical and γ-ray variations favours leptonic (i.e. inverse-Compton scattering of the optical photons as the production mechanism for the γ-ray emission) over hadronic processes. On the other hand, the fact that the radio usually lags all other wavelengths suggests that it is typically downstream from both the optical and γ-ray emission regions. Since the radio variations are connected to the ejection of new components from the radio core seen in VLBI maps (Savolainen et al. 2002), this would place the γ-ray emission regions between the supermassive black hole and the radio core. Combined with the generally longer time-scale variations seen at radio wavelengths (e.g. Hovatta et al. 2007), our results favour emission scenarios of an expanding disturbance propagating in the jet and becoming optically thin at higher frequencies before becoming transparent at radio wavelengths (e.g. Marscher & Gear 1985; Max-Moerbeck et al. 2014).

Using Bayesian block decomposition (Scargle et al. 2013), we have studied a large number of individual flares and their multi-wavelength properties. We have relied on the DCF analysis to align these light curves, allowing cross-band identification of individual flaring events. This has also for the first time allowed a robust determination of orphan (to our sensitivity) flares in all three wavebands.

Overall, sources showing a lower flaring rate tend to have less significant interband correlations, but this may be a simple selection effect. Comparing BL Lacs and FSRQs, the former show a higher flaring rate in the optical (3.6–3.7 versus 2.3–2.5 flares yr^{-1} source^{-1} on average), while showing lower radio (0.9–1 versus 1.1–1.3 flares yr^{-1} source^{-1}) and γ-ray (0.3–0.5 versus 0.6–0.8 flares yr^{-1} source^{-1}) activity.

Two main effects limit the present analysis. First, seasonal gaps in the optical light curves limit the number of flare identifications and make long-term trends difficult to follow. Although observational gaps in the optical are unavoidable because of the Sun, in many cases these are enlarged (or even induced) by weather and/or technical related constraints. Multisite monitoring could help minimize the extent of said gaps. Secondly, we have used only publicly accessible γ-ray light curves, with coarse 30 d sampling. As shown in Figs 5 and 7 (see also the discussion in Section 3), our overall statistical results and conclusions should not be strongly affected by the choice of bin size; however, finer sampling such as the adaptive binning used by Cohen et al. (2014) can find more flares and probe shorter time-scales. For this reason, our results on the flare rates and flare associations with respect to the γ-ray light curves should be treated as limits. We are currently pursuing a more detailed analysis of the γ-ray light curves that will allow us to probe time delays and flare associations on shorter time-scales between optical and γ-rays.

In summary, our results show the following:

(i) The radio emission generally lags the optical/γ-rays, suggesting that the higher energy radiation arises inwards of the radio cores of the jets.

[7]The WRS test is similar to the K-S test with the alternate hypothesis that one sample has systematically higher values than the other.

(ii) The optical emission is closely connected to the γ-ray emission, with roughly half the sources having time lags consistent with zero.

(iii) A few sources seem to have all three bands colocated (e.g. J0433+2905, J2236+2828).

(iv) Low radio and γ-ray activity likely explains the lack of significant correlation for many of our sources.

(v) We found no significant difference between associated and orphan γ-ray flares in sources with a significant γ-ray–radio correlation. In all other cases (and wavelengths), flares have higher flux when associated with the other band than when they are orphans.

ACKNOWLEDGEMENTS

We thank the anonymous referee and T. Hovatta for comments and suggestion that helped improve this work. The *Fermi* LAT Collaboration acknowledges generous ongoing support from a number of agencies and institutes that have supported both the development and the operation of the LAT as well as scientific data analysis. These include the National Aeronautics and Space Administration (NASA) and the Department of Energy in the United States, the Commissariat à l'Energie Atomique and the Centre National de la Recherche Scientifique/Institut National de Physique Nucléaire et de Physique des Particules in France, the Agenzia Spaziale Italiana and the Istituto Nazionale di Fisica Nucleare in Italy, the Ministry of Education, Culture, Sports, Science, and Technology (MEXT), High Energy Accelerator Research Organization (KEK), and Japan Aerospace Exploration Agency (JAXA) in Japan, and the K. A. Wallenberg Foundation, the Swedish Research Council, and the Swedish National Space Board in Sweden. Additional support for science analysis during the operations phase is gratefully acknowledged from the Istituto Nazionale di Astrofisica in Italy and the Centre National d'Études Spatiales in France.

This research has made use of data from the robotic 0.76-m Katzman Automatic Imaging telescope (Li et al. 2003) at Lick Observatory. We thank the late Weidong Li for setting up the KAIT blazar monitoring program. This work was financed in part by NASA grants NNX10AU09G, GO-31089, NNX12AF12G, and NAS5-00147. AVF and WZ are also grateful for support from the Christopher R. Redlich Fund, the TABASGO Foundation, NSF grant AST-1211916, and the Miller Institute for Basic Research in Science (UC Berkeley). KAIT and its ongoing operation were made possible by donations from Sun Microsystems, Inc., the Hewlett-Packard Company, AutoScope Corporation, Lick Observatory, the NSF, the University of California, the Sylvia and Jim Katzman Foundation, and the TABASGO Foundation. Research at Lick Observatory is partially supported by a generous gift from Google. This work has made use of data from the OVRO 40-m monitoring program (Richards et al. 2011), which is supported in part by NASA grants NNX08AW31G, NNX11A043G, and NNX14AQ89G, as well as by NSF grants AST-0808050 and AST-1109911. AVF's research was conducted in part at the Aspen Center for Physics, which is supported by NSF grant PHY-1607611. He thanks the Centre for its hospitality during the supermassive black holes workshop in 2018 June and July.

REFERENCES

Abdo A. A. et al., 2010a, ApJ, 715, 429
Abdo A. A. et al., 2010b, ApJ, 716, 30
Acero F. et al., 2015, ApJS, 218, 23
Blinov D. et al., 2018, MNRAS, 474, 1296
Bonning E. et al., 2012, ApJ, 756, 13
Chen X., Fossati G., Böttcher M., Liang E., 2012, MNRAS, 424, 789
Cohen D. P., Romani R. W., Filippenko A. V., Cenko S. B., Lott B., Zheng W., Li W., 2014, ApJ, 797, 137
Dermer C. D., Schlickeiser R., Mastichiadis A., 1992, A&A, 256, L27
Edelson R. A., Krolik J. H., 1988, ApJ, 333, 646
Filippenko A. V., Li W. D., Treffers R. R., Modjaz M., 2001, in Paczynski B., Chen W.-P., Lemme C. eds, Astronomical Society of the Pacific Conference Series Vol. 246, IAU Colloq. 183: Small Telescope Astronomy on Global Scales, Astron. Soc. Pac., San Francisco. p. 121
Fuhrmann L. et al., 2014, MNRAS, 441, 1899
Hovatta T., Tornikoski M., Lainela M., Lehto H. J., Valtaoja E., Torniainen I., Aller M. F., Aller H. D., 2007, A&A, 469, 899
Hovatta T. et al., 2014, MNRAS, 439, 690
Jorstad S. G. et al., 2017, ApJ, 846, 98
Karamanavis V. et al., 2016, A&A, 590, A48
Krawczynski H. et al., 2004, ApJ, 601, 151
Li W., Filippenko A. V., Chornock R., Jha S., 2003, PASP, 115, 844
Liodakis I. et al., 2017, MNRAS, 466, 4625
Lister M. L. et al., 2009, AJ, 138, 1874
Lott B., Escande L., Larsson S., Ballet J., 2012, A&A, 544, A6
Marscher A. P., Gear W. K., 1985, ApJ, 298, 114
Marscher A. P. et al., 2008, Nature, 452, 966
Max-Moerbeck W. et al., 2014, MNRAS, 445, 428
Patiño-Álvarez V., Carramiñana A., Carrasco L., Chavushyan V., 2013, preprint (arXiv:1303.1898)
Peterson B. M., Wanders I., Horne K., Collier S., Alexander T., Kaspi S., Maoz D., 1998, PASP, 110, 660
Ramakrishnan V., Hovatta T., Nieppola E., Tornikoski M., Lähteenmäki A., Valtaoja E., 2015, MNRAS, 452, 1280
Ramakrishnan V. et al., 2016, MNRAS, 456, 171
Rani B. et al., 2013, A&A, 552, A11
Richards J. L. et al., 2011, ApJS, 194, 29
Savolainen T., Wiik K., Valtaoja E., Jorstad S. G., Marscher A. P., 2002, A&A, 394, 851
Scargle J. D., Norris J. P., Jackson B., Chiang J., 2013, ApJ, 764, 167
Zhang B. K., Zhao X. Y., Zhang L., Dai B. Z., 2017, ApJS, 231, 14

APPENDIX: CROSS-CORRELATION RESULTS

Table A1. Cross-correlation results for the sources in our sample that showed a $>1\sigma$ significant DCF peak. Columns: (1) KAIT name, (2) class (B for BL Lacs, F for FSRQs), (3) redshift, (4) optical–radio time lag ($\tau_{o\text{-}r}$), (5) uncertainty of $\tau_{o\text{-}r}$, (6) significance of the peak DCF_{o-r} coefficient, (7) optical–γ-rays time lag ($\tau_{o\text{-}g}$), (8) uncertainty of $\tau_{o\text{-}g}$, (9) significance of the peak DCF_{o-g} coefficient, (10) γ-ray–radio time lag ($\tau_{g\text{-}r}$), (11) uncertainty of $\tau_{g\text{-}r}$, (12) significance of the peak DCF_{g-r} coefficient. For a positive $\tau_{o\text{-}r}$ or $\tau_{o\text{-}g}$, the optical emission is leading the radio or γ-rays, respectively; for a positive $\tau_{g\text{-}r}$ the γ-ray emission is leading the radio.

Name	Class	z	$\tau_{o\text{-}r}$	$\sigma\tau_{o\text{-}r}$	Signif. (DCF_{o-r})	$\tau_{o\text{-}g}$	$\sigma\tau_{o\text{-}g}$	Signif. (DCF_{o-g})	$\tau_{g\text{-}r}$	$\sigma\tau_{g\text{-}r}$	Signif. (DCF_{g-r})
(1)	(2)	(3)	(4)	(5)	(6)	(7)	(8)	(9)	(10)	(11)	(12)
J0017−0512	F	0.227	200.96	1.2	2.04	20.23	3.66	2.1	113.15	5.96	1.06
J0033−1921	B	0.61	–	–	–	–	–	–	–	–	–
J0035+1515	B	1.409	–	–	–	–	–	–	365.7	5.96	1.9
J0035+5950	B	0.086	–	–	–	15.11	0.0	1.01	221.9	29.41	2.43
J0045+2127	B	–	–	–	–	204.06	2.65	2.0	–	–	–
J0050−0929	B	0.635	–	–	–	-17.88	3.03	3.05	161.31	2.34	2.8
J0102+5824	F	0.644	270.71	2.26	2.2	-2.16	9.2	3.22	162.41	5.13	1.96
J0112+2244	B	0.265	–	–	–	7.11	4.0	2.53	–	–	–
J0115+2519	B	0.37	–	–	–	13.59	12.97	2.08	–	–	–
J0132−1654	F	1.02	–	–	–	-35.28	5.74	2.02	−12.76	9.7	1.13
J0136+3905	B	0.75	–	–	–	–	–	–	–	–	–
J0141−0928	B	0.733	−18.49	4.22	1.28	24.61	0.88	2.82	–	–	–
J0154+0823	B	0.681	178.02	0.22	1.0	–	–	–	343.01	12.08	2.47
J0204−1701	F	1.74	774.39	3.89	2.41	6.26	2.6	2.28	564.47	6.98	1.34
J0211+1051	B	0.2	−12.0	7.66	1.6	12.31	3.92	2.08	–	–	–
J0222+4302	B	0.34	240.33	3.72	3.22	27.0	1.5	3.0	400.56	29.91	1.31
J0237+2848	F	1.213	120.17	3.61	2.4	6.8	4.6	2.65	493.19	1.95	1.67
J0312+0133	F	0.664	–	–	–	–	–	–	–	–	–
J0316+0904	B	0.372	–	–	–	–	–	–	–	–	–
J0423−0120	F	0.915	–	–	–	−0.48	5.17	3.08	118.48	6.07	2.27
J0424+0036	B	0.266	–	–	–	–	–	–	–	–	–
J0433+2905	B	0.97	24.69	0.0	1.0	27.01	0.0	1.33	10.47	3.66	1.88
J0442−0017	F	0.844	−66.75	4.03	1.93	11.81	4.32	2.1	−549.1	1.67	1.17
J0507+6737	B	0.314	–	–	–	–	–	–	–	–	–
J0509+0541	B	–	–	–	–	−24.65	4.76	1.19	–	–	–
J0521+2112	B	0.108	98.61	11.09	2.66	−33.25	2.51	3.37	244.93	11.95	2.78
J0532+0732	F	1.254	77.72	3.4	1.82	−4.87	0.65	2.57	–	–	–
J0607+4739	B	–	293.17	4.58	1.52	–	–	–	–	–	–
J0612+4122	B	–	–	–	–	–	–	–	−75.37	2.71	2.05
J0648+1516	B	0.179	108.86	0.0	2.47	–	–	–	–	–	–
J0650+2502	B	0.203	–	–	–	–	–	–	–	–	–
J0654+5042	–	1.253	–	–	–	–	–	–	–	–	–
J0710+5908	B	0.125	–	–	–	–	–	–	–	–	–
J0725+1425	F	1.038	229.15	7.5	1.51	8.94	0.0	1.78	563.85	3.32	1.2
J0738+1742	B	0.424	51.16	3.93	2.65	2.03	10.78	3.47	96.62	18.67	1.45
J0739+0137	F	0.191	62.76	3.09	1.3	−0.89	6.62	2.0	–	–	–
J0742+5444	F	0.723	110.97	3.09	2.35	19.9	4.23	3.11	155.58	3.66	2.54
J0744+7433	B	0.314	–	–	–	–	–	–	328.12	0.0	1.19
J0750+1231	F	0.889	–	–	–	–	–	–	199.55	16.57	1.4
J0754−1147	–	–	188.55	0.13	2.14	–	–	–	300.39	0.0	1.78
J0757+0956	B	0.266	577.3	4.43	1.46	–	–	–	278.81	12.45	1.5
J0807−0541	B	–	–	–	–	–	–	–	–	–	–
J0808−0751	F	1.837	–	–	–	-9.35	0.14	1.82	119.27	7.21	2.47
J0809+5218	B	0.137	–	–	–	51.48	3.48	3.15	166.79	5.2	1.22
J0814+6431	B	0.239	249.79	3.65	2.05	9.28	1.52	2.5	–	–	–
J0816-1311	B	0.046	–	–	–	–	–	–	–	–	–
J0818+4222	B	0.53	–	–	–	1.47	6.35	2.0	217.02	4.87	1.81
J0824+5552	F	1.417	–	–	–	–	–	–	236.28	6.15	1.0
J0830+2410	F	0.94	–	–	–	-50.99	4.12	3.02	–	–	–
J0831+0429	B	0.174	609.16	4.79	1.23	7.23	10.21	1.31	678.41	5.78	1.29
J0850−1213	F	0.566	70.03	4.5	1.72	22.97	4.39	2.0	91.59	15.0	2.03
J0854+2006	B	0.306	187.16	4.8	1.57	–	–	–	591.64	8.9	1.9
J0856−1105	B	–	150.5	6.88	1.44	–	–	–	–	–	–
J0909+0121	F	1.024	95.94	8.12	3.1	−27.5	3.53	3.1	453.03	15.91	1.53
J0915+2933	B	1.521	–	–	–	–	–	–	−2.03	0.0	2.0
J0920+4441	F	2.19	–	–	–	6.55	16.43	1.1	−152.03	8.46	1.75
J0953−0840	B	0.59	–	–	–	–	–	–	–	–	–

Table A1 – *continued*

Name	Class	z	$\tau_{o\text{-}r}$	$\sigma\tau_{o\text{-}r}$	Signif. (DCF_{o-r})	$\tau_{o\text{-}g}$	$\sigma\tau_{o\text{-}g}$	Signif. (DCF_{o-g})	$\tau_{g\text{-}r}$	$\sigma\tau_{g\text{-}r}$	Signif. (DCF_{g-r})
(1)	(2)	(3)	(4)	(5)	(6)	(7)	(8)	(9)	(10)	(11)	(12)
J0957+5522	F	0.899	–	–	–	–	–	–	–	–	–
J1001+2911	B	0.08	250.82	12.07	2.05	7.82	23.42	2.0	241.14	6.28	2.5
J1015+4926	B	1.19	–	–	–	–	–	–	–	–	–
J1037+5711	B	0.831	−26.89	2.28	2.25	2.84	2.4	3.1	416.11	1.86	1.41
J1053+4929	B	0.14	–	–	–	–	–	–	–	–	–
J1058+0133	B	0.185	56.7	45.89	2.14	15.33	4.28	2.5	95.51	7.05	1.1
J1058+5628	B	0.143	–	–	–	14.35	11.19	2.63	–	–	–
J1059−1134	B	–	–	–	–	–	–	–	–	–	–
J1117+2014	B	0.138	–	–	–	–	–	–	–	–	–
J1130−1449	F	1.189	–	–	–	–	–	–	483.28	15.9	2.56
J1132+0034	B	0.678	–	–	–	−13.44	0.0	2.17	146.04	0.0	1.61
J1136+7009	B	0.046	–	–	–	–	–	–	–	–	–
J1150+4154	B	0.004	–	–	–	–	–	–	–	–	–
J1159+2914	F	0.729	–	–	–	30.57	10.2	1.6	89.83	6.67	1.65
J1217+3007	B	0.13	212.86	1.6	3.0	–	–	–	363.53	5.77	1.75
J1221+2813	B	0.102	–	–	–	−8.46	7.79	1.6	–	–	–
J1221+3010	B	0.184	–	–	–	–	–	–	–	–	–
J1222+0413	F	0.965	13.53	74.7	1.06	–	–	–	177.49	3.43	1.7
J1224+2122	F	0.434	58.38	17.18	2.1	−23.41	7.13	2.12	–	–	–
J1231+2847	B	0.236	–	–	–	–	–	–	–	–	–
J1243+3627	B	1.066	–	–	–	–	–	–	–	–	–
J1248+5820	B	0.847	156.83	4.1	1.62	28.91	8.73	2.11	–	–	–
J1253+5301	B	1.084	–	–	–	13.51	8.95	2.21	–	–	–
J1256−0547	F	0.536	31.38	3.96	2.37	−49.95	11.5	1.9	–	–	–
J1309+4305	B	0.691	–	–	–	–	–	–	–	–	–
J1310+3220	F	0.997	−12.83	2.23	1.26	237.56	10.7	1.44	–	–	–
J1314+2348	B	1.54	103.56	4.19	2.63	−43.35	7.81	3.37	–	–	–
J1337−1257	F	0.539	–	–	–	–	–	–	−329.91	4.31	1.65
J1351+1114	B	0.395	–	–	–	–	–	–	–	–	–
J1354−1041	F	0.332	–	–	–	31.53	3.7	1.9	679.99	0.94	1.33
J1418−0233	B	0.0	15.13	7.4	2.45	55.1	14.22	3.17	161.88	15.15	1.57
J1427+2347	B	0.16	–	–	–	−33.43	7.06	2.28	–	–	–
J1428+4240	B	0.129	–	–	–	–	–	–	–	–	–
J1436+5639	B	0.17	–	–	–	–	–	–	–	–	–
J1440+0610	B	0.396	–	–	–	–	–	–	67.68	10.41	2.3
J1448+3608	B	1.508	–	–	–	–	–	–	–	–	–
J1501+2238	B	0.235	71.02	0.0	2.01	–	–	–	437.02	5.37	1.33
J1505+0326	–	–	–	–	–	–	–	–	91.83	16.57	2.25
J1542+6129	B	0.507	–	–	–	−0.99	2.54	2.37	–	–	–
J1549+0237	F	0.414	–	–	–	–	–	–	–	–	–
J1553+1256	F	1.308	–	–	–	–	–	–	–	–	–
J1555+1111	B	0.36	127.48	1.84	1.44	10.03	12.38	2.04	93.89	25.53	1.94
J1558+5625	B	0.3	–	–	–	–	–	–	107.4	5.58	1.46
J1608+1029	F	1.226	–	–	–	–	–	–	68.85	1.88	1.51
J1635+3808	F	1.814	18.95	5.92	1.46	−21.26	6.72	2.16	52.61	2.05	2.41
J1642+3948	F	0.593	26.13	1.92	2.04	85.37	8.46	1.0	−304.31	2.75	1.36
J1643−0646	–	0.082	–	–	–	–	–	–	−323.73	0.65	1.71
J1719+1745	B	0.137	–	–	–	19.25	13.59	2.0	–	–	–
J1725+1152	B	0.018	–	–	–	–	–	–	239.21	0.0	1.02
J1725+5851	B	0.001	–	–	–	–	–	–	269.73	0.0	3.12
J1727+4530	F	0.714	–	–	–	–	–	–	255.15	13.38	1.52
J1740+5211	F	1.379	–	–	–	186.11	1.7	1.78	–	–	–
J1748+7005	B	0.77	426.14	3.13	1.0	14.64	7.97	3.23	88.21	25.94	1.23
J1751+0939	B	0.322	–	–	–	–	–	–	–	–	–
J1754+3212	B	1.09	–	–	–	12.14	7.2	3.0	163.12	9.59	2.46
J1800+7828	B	0.68	–	–	–	4.79	6.66	3.02	96.26	8.75	1.0
J1813+3144	B	0.117	–	–	–	–	–	–	–	–	–
J1824+5651	B	0.664	–	–	–	7.65	5.9	2.13	–	–	–
J1849+6705	F	0.657	30.33	2.96	1.22	-3.86	4.85	2.68	40.74	15.67	1.0

Table A1 *– continued*

Name	Class	z	$\tau_{o\text{-}r}$	$\sigma\tau_{o\text{-}r}$	Signif. (DCF_{o-r})	$\tau_{o\text{-}g}$	$\sigma\tau_{o\text{-}g}$	Signif. (DCF_{o-g})	$\tau_{g\text{-}r}$	$\sigma\tau_{g\text{-}r}$	Signif. (DCF_{g-r})
(1)	(2)	(3)	(4)	(5)	(6)	(7)	(8)	(9)	(10)	(11)	(12)
J1903+5540	B	0.58	66.45	1.02	1.54	5.03	3.51	2.47	161.91	10.31	1.74
J1917−1921	B	0.137	289.78	3.05	4.9	39.54	21.9	1.57	-8.29	5.9	1.6
J1921−1607	B	–	–	–	–	–	–	–	–	–	–
J1926+6154	B	–	–	–	–	–	–	–	–	–	–
J1959+6508	B	0.049	−51.91	0.56	3.21	−5.49	6.09	1.01	–	–	–
J2000−1748	F	0.652	12.82	2.35	2.05	–	–	–	−13.05	3.76	2.03
J2012+4628	B	–	466.61	1.19	1.36	7.35	6.44	3.03	511.51	4.84	2.45
J2039−1046	B	1.05	221.13	0.87	2.6	–	–	–	–	–	–
J2055−0021	B	0.407	–	–	–	–	–	–	–	–	–
J2116+3339	B	1.596	–	–	–	–	–	–	264.15	16.91	3.01
J2143+1743	F	0.211	–	–	–	–	–	–	615.35	18.14	1.55
J2147+0929	F	1.113	170.1	2.99	1.75	17.3	0.0	1.0	–	–	–
J2152+1734	B	0.871	–	–	–	–	–	–	–	–	–
J2202+4216	B	0.069	–	–	–	−7.78	5.58	2.01	–	–	–
J2203+1725	F	1.076	–	–	–	–	–	–	553.88	3.27	2.16
J2225−0457	F	1.404	255.3	0.05	1.01	–	–	–	225.48	7.48	2.27
J2229−0832	F	1.559	239.34	5.44	1.2	25.84	9.03	1.0	62.09	15.75	1.74
J2232+1143	F	1.037	300.3	0.3	2.17	24.49	1.32	3.12	–	–	–
J2236−1433	B	0.325	718.5	2.74	1.71	25.27	8.0	3.26	715.5	1.35	1.12
J2236+2828	F	0.795	11.73	3.14	1.28	−2.11	15.03	2.5	−4.72	5.43	1.01
J2243+2021	B	0.39	–	–	–	78.26	14.17	1.34	–	–	–
J2250+3824	B	0.119	–	–	–	–	–	–	–	–	–
J2251+4030	B	0.229	–	–	–	–	–	–	–	–	–
J2253+1608	F	0.859	402.95	5.93	2.36	−5.72	2.77	2.57	115.49	5.85	2.5
J2323+4210	B	0.059	–	–	–	–	–	–	–	–	–
J2329+3754	–	0.264	–	–	–	–	–	–	–	–	–
J2345−1555	F	0.621	20.58	0.97	2.38	−11.58	0.0	3.36	93.82	1.32	2.06
J2347+5142	B	0.044	57.37	0.0	1.35	−13.36	28.62	1.01	100.96	1.57	2.04
J2348−1631	F	0.576	–	–	–	–	–	–	–	–	–

This paper has been typeset from a TEX/LATEX file prepared by the author.